Deep-Sea Research Part I 132 (2018) 80–93

Contents lists available at ScienceDirect

Deep-Sea Research Part I

journal homepage: www.elsevier.com/locate/dsri

Impacts of two super typhoons on the Kuroshio and marginal seas on the Pacific coast of Japan

Hiroaki Tada[a,1], Yusuke Uchiyama[a,c,*], Eiji Masunaga[b]

[a] Department of Civil Engineering, Kobe University, Kobe, Japan
[b] Center for Water Environment Studies, Ibaraki University, Hitachi, Japan
[c] Coastal and Estuarine Environmental Department, Port and Airport Research Institute, Yokosuka, Japan

ARTICLE INFO

Keywords:
Typhoon
Kuroshio
Near-inertial oscillation
Eddy shedding
Topography
Regional Oceanic Modeling System

ABSTRACT

High-resolution downscaling ocean modeling was conducted to investigate the impacts of two super typhoons on the Kuroshio in the fall of 2014 off the Kyushu and Shikoku Islands, Japan. The model result was compared with field observations and satellite altimetry. The synoptic and mesoscale oceanic structures around the Kuroshio exhibit a good reproducibility. The typhoons generated near-inertial oscillations (NIOs) and near-inertial internal waves (NIIWs) around the Kuroshio path, particularly on the right side of the typhoon tracks. The NIOs developed in the mixed layer to alter the direction of the Kuroshio by ~30°. The associated velocity off the Shikoku and Kyushu Islands was significantly decelerated by ~0.2 ms^{-1}. The velocity almost vanished off Kyushu Island and thus induced an unstable fluctuating path shortly after both typhoons passed over that region. The NIIWs were also excited at the thermocline, resulting in the oscillation of the Kuroshio path occurred in the entire water column. In contrast, off Shikoku Island, the typhoons shifted the Kuroshio path northward to enhance the interactions with the topographies. This shift caused considerable eddy shedding from the capes that resulted in mesoscale counterclockwise circulations as cyclonic quasi-standing eddies with a shedding period of ~3 days in the north of the Kuroshio path. The magnitude, direction, and meridional location of the path of the Kuroshio prominently fluctuated with the propagation of these eddies, manifested off Shikoku Island. Furthermore, these eddies induced sporadic northward intrusions of the Kuroshio warm water through the Kii Channel into the Seto Inland Sea (SIS), where a weak but persisting southward outflow prevails under normal conditions. Therefore, the process could collectively be called the "typhoon-Kuroshio-eddy interaction", which conceptually differs from the "typhoon-eddy-Kuroshio interaction" in the previous studies, where the Kuroshio was modulated by eddy collision. The wind stress curl and intrusions associated with the typhoons jointly provoked the inversion of the counterclockwise SIS residual circulation. The resultant spatially averaged volume flux was ~8 times as high as that under normal conditions.

1. Introduction

The Kuroshio is the western boundary current of the North Pacific Subtropical Gyre, which transports massive amounts of heat and salinity from lower latitudes to middle and high latitudes. The Kuroshio generally flows on the continental shelf break around Japan, while its path is not always persistent but rather transient. For instance, the Kuroshio typically takes either of the three paths off the Cape Shionomisaki (Fig. 1): 1) nearshore straight (*i.e.*, non-large-meander), 2) offshore straight, or 3) large-meander paths (*e.g.*, Kawabe, 1985, 1995; Akitomo et al., 1991; Miyazawa et al., 2008, 2009). At the Tokara Strait, the Kuroshio initiates its meandering either by a large inflow (*e.g.*, Nakamura et al., 2006), a small path meander (*e.g.*, Kawabe, 1995; Miyazawa et al., 2008), low potential vorticity (PV) water (*e.g.*, Qiu and Miao, 2000), or high PV water (*e.g.*, Akitomo and Kurogi, 2001).

The Kuroshio and its path are potentially influenced by typhoons. Typhoons magnify the vertical mixing and Ekman transport due to the strong surface wind stress, decrease the sea surface temperature (SST), and alter the upper-ocean circulations (*e.g.*, Yang and Sheng, 2008). Inertial oscillations associated with typhoons are also known to be intense with velocity magnitudes as large as 1 ms^{-1} (*e.g.*, Price, 1981; Church et al., 1989), which is comparable to the mean velocity of the Kuroshio. Based on the surface currents observed by radars, Morimoto et al. (2009) reported that typhoons occasionally alter the current

* Corresponding author at: Department of Civil Engineering, Kobe University, Kobe, Japan.
E-mail addresses: a8365@n-koei.co.jp (H. Tada), uchiyama@harbor.kobe-u.ac.jp (Y. Uchiyama), eiji.masunaga.office@vc.ibaraki.ac.jp (E. Masunaga).
[1] Present address: Nippon Koei Co. Ltd., Tokyo, Japan.

https://doi.org/10.1016/j.dsr.2017.12.007
Received 17 March 2017; Received in revised form 22 December 2017; Accepted 24 December 2017
Available online 29 December 2017
0967-0637/

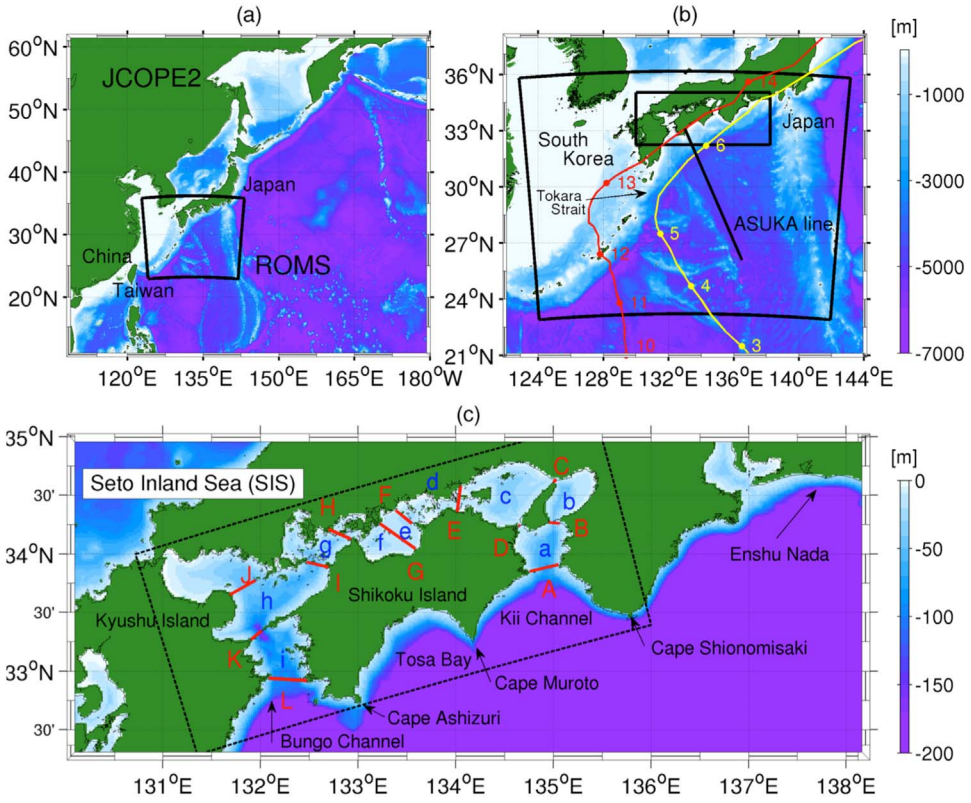

Fig. 1. The study area with bathymetry in color (m). (a) Entire JCOPE2 domain with the embedded child ROMS model domain (black box). (b) Blow-up of the ROMS domain indicated by the black box in (a) corresponding to the outer black box in (b). (c) Blow-up around the Seto Inland Sea (SIS) shown by the inner black box in (b). The black dashed box in (c) indicates the approximate extent of the SIS. In (b), the best tracks of Phanfone (yellow line) and Vongfong (red line) are overlaid; the typhoon days in October 2014 in UTC are indicated. The black bold line in (b) represents the JMA ASUKA Line transect used for Fig. 3. In (c), the red bold lines with the red capital letters A-L are the transects used for Fig. 11; with the lowercase letters *a-i* are the segments used for Table 2. (For interpretation of the references to color in this figure legend, the reader is referred to the web version of this article.)

speed, direction, and axis of the Kuroshio off Taiwan due to the geostrophic currents enhanced by the sea surface height (SSH) gradient associated with the typhoon passages. Sun et al. (2009) reported that the typhoon-induced localized upwelling intensifies the preexisting cyclonic eddies, giving rise to a large meander of the Kuroshio off Shikoku Island. Such alterations of the Kuroshio path affect not only the coastal environment and ecosystem (*e.g.*, Nakata et al., 2000; Yang et al., 2010; Sun et al., 2012) by changing the water temperature and SSH (*e.g.*, Kawabe, 1985) but also the heat balance in the lower atmospheric boundary layer through the intensive eddy-current and air-sea interactions along the Kuroshio path (*e.g.*, Qiu, 2003; Taguchi et al., 2005; Tanimoto et al., 2009; Tokinaga et al., 2009), which consequently leads to feedback on the intensity and fate of the typhoons.

The transient Kuroshio substantially influences an extensive portion of the coastal waters on the Pacific side of Japan, including the Seto Inland Sea (SIS). The SIS is the largest semi-enclosed estuary in the nation, zonally stretching over ~450 km, with widths of 15–55 km, bounded by the Honshu, Shikoku, and Kyushu islands (Fig. 1). The Bungo Channel to the west and the Kii Channel to the east connect the SIS to the Pacific. The transient Kuroshio occasionally causes sporadic intrusions of the Kuroshio into the Bungo Channel (Isobe et al., 2010), which is often referred to as "*kyucho*" (Takeoka and Yoshimura, 1988). The strong currents and abrupt temperature increase associated with *kyucho* result in serious damage of fishery nets and fish cultivations (*e.g.*, Takeoka and Yoshimura, 1988; Matsuyama et al., 1997). In addition, typhoons pass over or around the SIS several times a year, mostly every fall. Hence, possible dynamical impacts of typhoons on the Kuroshio and coastal water around the SIS due to the shift of the Kuroshio path are anticipated; however, they are poorly understood.

In the present study, we focus on two consecutive super typhoons that passed over and close to the SIS in the fall of 2014. The first one is Typhoon Phanfone with an intensity of category 4 and the lowest sea level pressure (SLP) of 935 hPa; the second one is Typhoon Vongfong, the most powerful typhoon in 2014, with category 5 and the lowest SLP of 900 hPa. Both are known to have altered the Kuroshio path off the Kii Channel based on the SST composite maps (Section 5.1). We aim to clarify the oceanic responses to the two typhoons and pay particular attention to their impact on the Kuroshio and the SIS circulation. We conducted retrospective, high-resolution downscaling ocean modeling using the Regional Oceanic Modeling System (ROMS; Shchepetkin and McWilliams, 2005, 2008) embedded in the Japan Coastal Ocean Predictability Experiment version 2 (JCOPE2) assimilative oceanic reanalysis (Miyazawa et al., 2009) forced by the high-resolution Grid Point Value-Mesoscale Model (GPV-MSM) assimilative atmospheric product (*e.g.*, Isoguchi et al., 2010). The ROMS model domain extends over a fairly wide area, particularly southward, to encompass typhoons from their early stage at lower latitudes. The ROMS horizontal grid spacing is 2 km, which marginally resolves the complicated topography and islands in the SIS.

The remainder of this paper is organized as follows. The model configuration is described in Section 2, followed by a comparison of the model results with field observations and satellite altimetry for validation in Section 3. We estimate the development of near-inertial oscillations (NIOs) and near-inertial internal waves (NIIWs) due to the typhoon, mainly in the open ocean in Section 4. Subsequently, influences of the typhoons on the Kuroshio path and the adjacent coastal waters including the SIS are discussed in Section 5. In Section 6, we analyze the possible mechanisms of the typhoons altering the Kuroshio path and the resultant topographic eddy shedding that recursively feeds back to modify the Kuroshio at the continental shelf margins. Then the conclusions are given in Section 7.

2. The model

The hydrodynamic model we use is the ROMS, a 3D hydrostatic Primitive equation ocean circulation model based on the Boussinesq approximation. To accurately account for the effects of the typhoons, the inverse barometer associated with the SLP anomaly is introduced in the pressure gradient term. The GPV-MSM assimilative atmospheric product of the Japan Meteorological Agency (JMA) with a horizontal

resolution of ~5 km is used for the determination of the surface momentum, heat, freshwater, and radiation fluxes based on the Coupled Ocean/Atmosphere Mesoscale Prediction System (COAMPS; Hodur, 1997) bulk formula. Note that the shortwave solar radiation is replaced with the composite of the *in situ* data provided by JMA for better reproducibility. Tides, wind waves, and swells are omitted for simplicity. The vertical eddy mixing of the momentum, heat, and scalar (salinity) in the surface and bottom boundary layers is evaluated with the K-profile Parameterization (KPP) turbulence model (Large et al., 1994; Durski et al., 2004).

The ROMS model domain horizontally extends 1840 km × 1440 km with a lateral grid spacing of 2 km to encompass a sufficiently wide area that includes as much tracks of the two typhoons as possible (Fig. 1), and is represented by vertically stretched 32 *s*-layers, where grid height refinement occurs near the surface to range *O* (0.1–2 m) for the topmost grid cells. The daily averaged JCOPE2 reanalysis (Miyazawa et al., 2009) with a lateral grid spacing of ~10 km is used as the initial and open boundary conditions. The ROMS model is embedded in the JCOPE2 to convey the basin-scale information into the child ROMS domain with the one-way offline nesting approach, as described in Mason et al. (2010) and Uchiyama et al. (2017a, 2017b). The model topography is obtained from the SRTM30_Plus (Rodriguez et al., 2005; Becker et al., 2009), which covers the global ocean at 30 geographic arc seconds or approximately 1 km supplemented by the J-EGG500 at a resolution of 0.5 km for the coastal regions. The other boundary condition, in particular the sea surface salinity (SSS) to correct the long-term bias in the freshwater flux, is imposed using the monthly SSS climatology of the NOAA-COADS (Woodruff et al., 1987) dataset. The major river discharges into the domain are considered based on the monthly climatology dataset provided by the Japan River Association. Four-dimensional nudging (also known as robust diagnostic; *e.g.*, Marchesiello et al., 2003) with a weak nudging inverse time scale of $1/20\ \mathrm{day}^{-1}$ is applied towards the 10-day averaged JCOPE2 3D temperature and salinity fields to enhance the reproducibility of the Kuroshio path. The ROMS model runs for 24 months including the initial spin-up for 18 month. For the following analyses, we mainly utilize the result for the three-month period from September 1, 2014. The numerical configurations are summarized in Table 1.

3. Validation

We compare the model results with the satellite altimetry, SST data, and *in situ* observations conducted by JMA to confirm the validity and reproducibility of the present ROMS model. The mean structure and temporal variability of the near-surface currents including the Kuroshio and its path are obtained from the gridded composite of multiple satellite altimetry data compiled by AVISO (*e.g.*, Traon et al., 1998). The delayed-time SSH anomaly data is available daily, with a horizontal spacing of 1/4°. Although this data set has recently been reprocessed as the DUACS/AVISO DT14 (Pujol et al., 2016), we rely on the previous version because it has extensively been used in the previous studies for model validations (*e.g.*, Uchiyama et al., 2017a, 2017b). The near-surface velocity magnitude and the Kuroshio path visualized by the time-averaged geostrophic current estimated from the AVISO-SSH exhibit a reasonable agreement with those of the JCOPE2 and ROMS (Fig. 2**a**, left column).

The SSH variance (Fig. 2**b**, middle column) is regarded as a proxy that measures the intensity of the temporal variability of synoptic and mesoscale signals mostly due to eddies and Kuroshio meanders. The ROMS-derived SSH variance reproduces several important features with magnitudes and spatial distributions equivalent to the AVISO data. For instance, an energetic area commonly arises north of 29°N off the southeast coast of Kyushu Island between 131°E and 133°E, where the westward-traveling Rossby waves and mesoscale eddies collide with the topographic ridge, giving rise to a large meander of the Kuroshio. The SSH variance is then enhanced pronouncedly in the wide area around 32°N between 137°E and 141°E off the Enshu-nada Sea, where the large meanders of the Kuroshio often occur. On the other hand, the SSH variance off Shikoku Island between 133°E and 136°E is relatively small, demonstrating that the Kuroshio path off Shikoku Island is rather stable.

Subsequently, the annual mean SST distribution is compared with the Merged satellite and *in situ* data Global Daily SST (MGDSST) of JMA, as shown in Fig. 2**c** (right column). The MGDSST is the gridded composite SST product at 1/4° including the AVHRR sensor of NOAA and MetOp satellites, AQUA/AMSR-E microwave satellite, and *in situ* SST data (Sakurai et al., 2005). Overall, the ROMS SST agrees reasonably well with that of the MGDSST and JCOPE2 with respect to the SST distribution including the location of the Kuroshio represented by warmer biases. However, the ROMS SST is slightly underestimated by about 1–2 °C compared with that of the MGDSST, particularly in the north of ~30°N on the Pacific side of Japan. It is worth noting that the parent JCOPE2 model already contains this underestimation on which the reproducibility of the ROMS model substantially depends (Section 2).

The modeled stratification is compared with *in situ* observations in the vertical cross section along the Affiliated Surveys of the Kuroshio off Cape Ashizuri (ASUKA) Line transect (*e.g.*, Imawaki et al., 2001), shown as black line in Fig. 1**b**. Ship-based hydrographic measurements along the ASUKA Line have been collected by a total of 155 cruises since November 1992 to evaluate the seasonal climatology of the density field (Fig. 3). Again, the ROMS model successfully reproduces the stratification for fall in terms of the depths and slopes of the isotherms and isohalines, with meridional northward steepening of the slopes. A minor discrepancy is observed for the subsurface salinity centered at 800-m depth, with an overestimation of ~0.1 PSU, whereas it arises from the parent JCOPE2 model similarly to the SST bias (Fig. 2**c**). Because the density in this region is mainly determined by the temperature rather than by salinity, the influence of the salinity deficiency on the general oceanic structure is presumed to be subtle.

The above validations are conducted rather in longer-time scales than near-inertial periods (Section 4), due primarily to the lack of sufficient data. However, we have validated high frequency reproducibility of the similar modeling in Buijsman et al. (2012), Kumar et al., (2015, 2016), Marchesiello et al. (2015) and Kamidaira et al. (2018), albeit at different sites and periods of time. In addition, the ROMS model has been applied by other modelers to the Gulf Stream region under hurricane conditions (*e.g.*, Xue et al., 2015; Mooney et al., 2016), as well as to the Kuroshio region under a typhoon condition (*e.g.*, Glenn et al., 2016) to confirm a good agreement with observation. Therefore, the present ROMS model is presumed to be capable of reproducing the overall 3D oceanic structure reasonably well under a typhoon condition in the study area.

Table 1
Computational configurations for the present ROMS model.

Computational period	1/1/2013–12/31/2014
Grid cells	920 × 720 × 32 vertical *s*-layers
Horizontal grid resolution	2.0 km
Baroclinic time step	120 s
Sea surface fluxes	JMA GPV-MSM (2 hourly) + COADS (monthly clim.)
Short-wave solar radiation	JMA *in situ* observation
Major river discharges	Japan River Association (monthly climatology)
Boundary and initial conditions	JCOPE2 (daily averaged)
T-S nudging	JCOPE2 (10-day averaged)
Topography	SRTM30 (SIO) supplemented by J-EGG500
Vertical eddy mixing	KPP model (Large et al., 1994)

4. Near-inertial motions driven by typhoons

We define fluctuations in the model results for the 21–30 h period

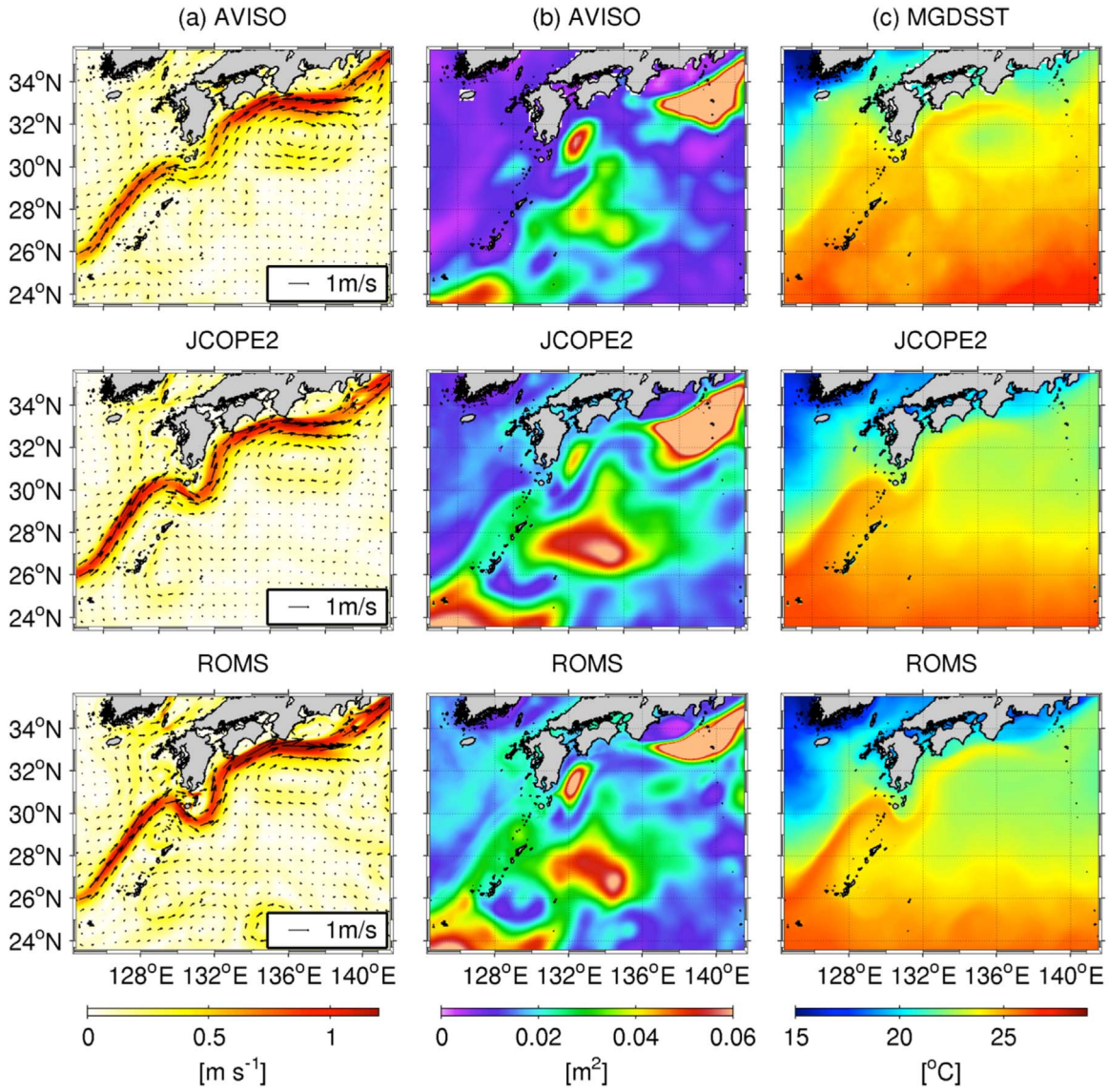

Fig. 2. Plan view plots of the annually averaged (a) surface velocity vectors and their magnitude in color, (b) sea-surface height (SSH) variance, and (c) sea-surface temperature (SST) for 2014. The top panels in (a) and (b) are based on the AVISO data, while the SST in (c) are based on the MGDSST. The middle panels are based on the JCOPE2, while the bottom panels show the ROMS model result.

band as the near-inertial component because the inertial period in the model domain ranges between 20.3–30.8 h. A Butterworth frequency band pass filter is applied to extract the near-inertial band in the meridional and zonal components of the horizontal current velocities, temperature, and salinity. Figure 4 indicates the instantaneous eddy kinetic energy, EKE $= (u'^2 + v'^2)/2$, and temperature anomalies, T', at the depths of 5, 30, and 100 m. Note that u and v are the zonal and meridional velocities, T is temperature, and the prime denotes the bandpass-filtered near-inertial fluctuating component. When Phanfone comes close to Shikoku Island, EKE is enhanced near the surface down to 30 m over a wide area, mostly on the right side of the track (Fig. 4**a**). Two days later, the area with near-surface high EKE extends northeastward and increases in the coastal sea and in the open ocean (Fig. 4**b**). The EKE barely extends and reaches a depth of 100 m, even after Phanfone passed. In contrast, the temperature anomaly is more apparent at 100-m depth, where deepening of the thermocline associated with the enhanced vertical mixing occurs along the typhoon track (not shown here, but partially evident in Fig. 8). It is conceivable that NIIWs with an amplitude of approximately 0.4 °C are generated below the typhoon track. These results suggest that the surface-concentrated EKE is barely transported below the thermocline and mostly dissipates in the mixed layer above a depth of 100 m, where the NIIWs develop. It is worth mentioning that the NIIWs in Fig. 4 might slightly be underestimated in the higher latitude with larger f with our choice of the frequency filter, which would be a bit narrow for encompassing modulations of the NIIWs as specified by the dispersion relation.

To assess the generation, horizontal propagation, and dissipation of the NIIWs, we calculate the baroclinic energy flux (*e.g.*, Nash et al., 2005) around the inertial period. The depth-integrated near-inertial baroclinic energy flux, $\boldsymbol{F}$, can be estimated from a correlation between the perturbation of the baroclinic velocity and pressure as follows:

$$\boldsymbol{F} = \left(\int_{-h}^{\eta} u'_{bc} p' dz,\ \int_{-h}^{\eta} v'_{bc} p' dz \right), \tag{1}$$

$$p'(z) = p_0 + g \int_{z}^{\eta} \rho'(\hat{z},\ T',\ S') d\hat{z} \tag{2}$$

where h is the depth; η is the sea surface height (SSH); $(u_{bc},\ v_{bc})$ are the baroclinic component of the horizontal velocities defined as residuals after subtracting the depth-averaged velocity; $(u'_{bc},\ v'_{bc})$ are the

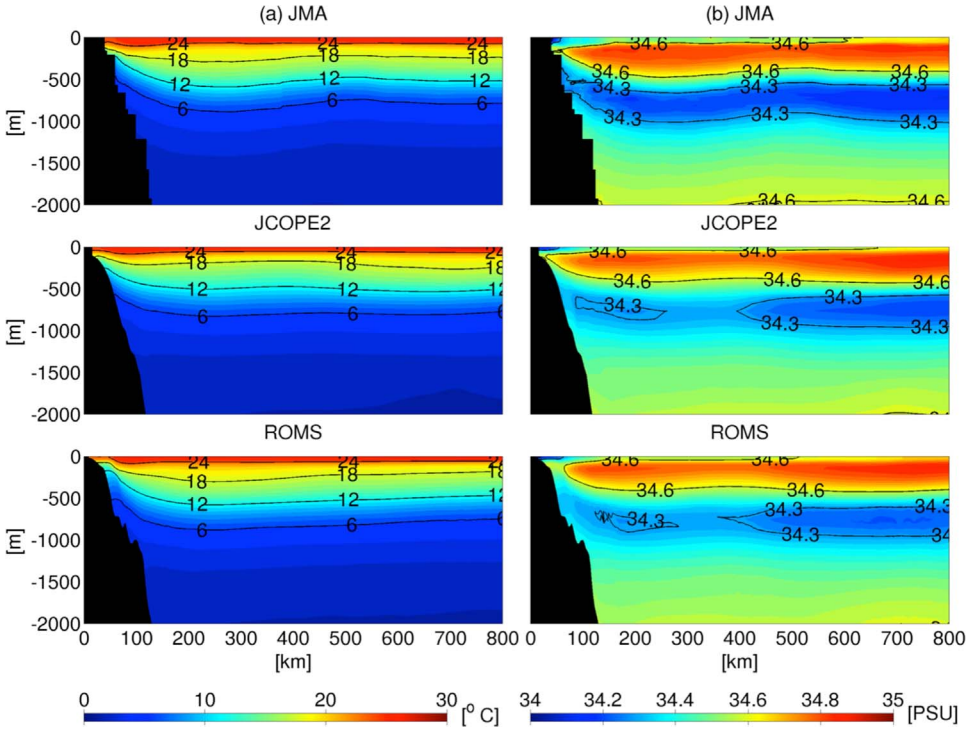

Fig. 3. Seasonally averaged (a) temperature and (b) salinity for fall from JMA *in situ* observations (top), JCOPE2 (middle), and the present ROMS model (bottom) in the vertical cross section along the ASUKA Line transect (Fig. 1**b**).

perturbation of (u_{bc}, v_{bc}); p' is the pressure perturbation; p_0 is the SLP assumed to be zero; g is the gravity; ρ is the density of the sea water, S is the salinity; z is the vertical axis with the mean sea level as origin, upward-positive; $\hat{z}$ is a dummy variable for the integral calculus; and the prime denotes the bandpass-filtered near-inertial component. Note that the pressure work is about three orders of magnitude larger than kinetic energy flux, and thus we omit the later in the present analysis.

The magnitude of both components of $\boldsymbol{F}$ averaged over the black rectangular off Shikoku Island shown in Fig. 5**b-c** considerably increases for ~10 days after Vongfong passes and dissipates gradually for more than one month (Fig. 5**a**). The comparison of the spatial distribution of $\boldsymbol{F}$ and its divergence (div $\boldsymbol{F}$) averaged for a non-typhoon period (*i.e.*, September 2014; Fig. 5**b** and **d**) and the period including the two typhoons (*i.e.*, October 2014; Fig. 5**c** and **e**) reveals that the typhoons intensify $\boldsymbol{F}$ by ~1 kW m^{-1} in extensive areas, particularly on the right side of the tracks, compared with the non-typhoon period. This 1 kWm^{-1} is dynamically substantial because it reaches approximately half of the baroclinic energy flux of energetic internal tides evaluated for Monterey Bay, California (Fig. 6 in Kang and Fringer, 2012). The vectors of $\boldsymbol{F}$ off Shikoku Island show that the baroclinic flux develops mainly southward, as if it moves away from the Kuroshio and turns clockwise (*e.g.*, in the area of the black box). Conversely, the baroclinic flux $\boldsymbol{F}$ moves to the Kuroshio in the south of Kyushu Island at ~132°E and 29°N while it is intensified by the two typhoons. This area corresponds to a bend of the Kuroshio path at which the flow direction considerably changes (Fig. 2**a**). The divergence of $\boldsymbol{F}$ (div $\boldsymbol{F}$; Fig. 5**e**) is consistently distributed with a strong convergence (*i.e.*, negative div $\boldsymbol{F}$) near these two areas (denoted by the black and green boxes in Fig. 5**e**) where the NIIWs are supposed to dissipate locally. For the non-typhoon period, $\boldsymbol{F}$ along the Kuroshio is divergent in the north (*e.g.*, K_1), while it is convergent in the south (*e.g.*, K_2) (Fig. 5**d**). This meridional div $\boldsymbol{F}$ pattern is enhanced for the typhoon period with an evident appearance of the positive div $\boldsymbol{F}$ to generate the southward propagating NIIWs in the south of the Kuroshio at ~135°E and 32°N (northwest area in the black box). In turn, the positive div $\boldsymbol{F}$ is not apparent in the south of Kyushu Island, where a negative div $\boldsymbol{F}$ is predominant. Therefore, the NIIWs lose their energy around the Kuroshio off Kyushu Island, whereas they extract baroclinic energy from the Kuroshio off Shikoku Island. As a result, it is anticipated that the Kuroshio path is altered by interactions with the energetic NIIWs associated with typhoons. A further investigation is needed for determining the mechanism in future works.

5. Influences on the Kuroshio and coastal waters

5.1. Modification of the Kuroshio by the typhoons

The observation supports that a typhoon can alter the path and structure of the Kuroshio off Shikoku Island through interactions of the typhoon with the associated eddies (*i.e.,* the typhoon-eddy-Kuroshio interaction; Sun et al., 2009). The fishery department of the Mie Prefecture, Japan, releases the daily averaged Kuroshio path off the Kii Channel inferred from satellite and *in situ* surface temperature and current data including those reported by fishery boats and research vessels, as shown in Fig. 6 for the period of the two typhoons. The Kuroshio path largely meanders northward to be oriented towards the Kii Channel after the passage of both typhoons. Fig. 7 shows the monthly averaged surface velocity vectors and their magnitude for the non-typhoon (September 2014) and typhoon (October 2014) periods based on the model. The faster flow shown by reddish colors represents the Kuroshio path, which decelerates by ~0.2 ms^{-1} due to the two consecutive typhoons on the south and east coasts off Kyushu Island encompassing the offshore area of the Bungo Channel around 132°E and 32°N. The deceleration is also evident in the time series of the streamwise northward velocity averaged over the EK Line (Fig. 8**a**). Immediately after Phanfone passes the EK Line on October 5, the streamwise velocity begins to oscillate pronouncedly in and below the mixed layer at a period of ~24 h (*i.e.*, near-inertial period). The mixed layer has deepened since October 3 to 75–80 m with fluctuations at the near-inertial period. The velocity averaged in the vertical, from the surface to the depth of 80 m (Fig. 8**c**), also demonstrates near-inertial periodic fluctuations after the passage of Phanfone, with an apparent deceleration bias of approximately −0.4 ms^{-1}. This deceleration is not a near-surface process, but occurs rather barotropically down to deeper than 400 m at least, with modest deepening of the Kurhoshio core from ~80 m to ~100 m depth (not shown). In contrast, the Kuroshio is less transient off Tosa Bay (TB Line, Fig. 8**b** and **d**), suggesting that the

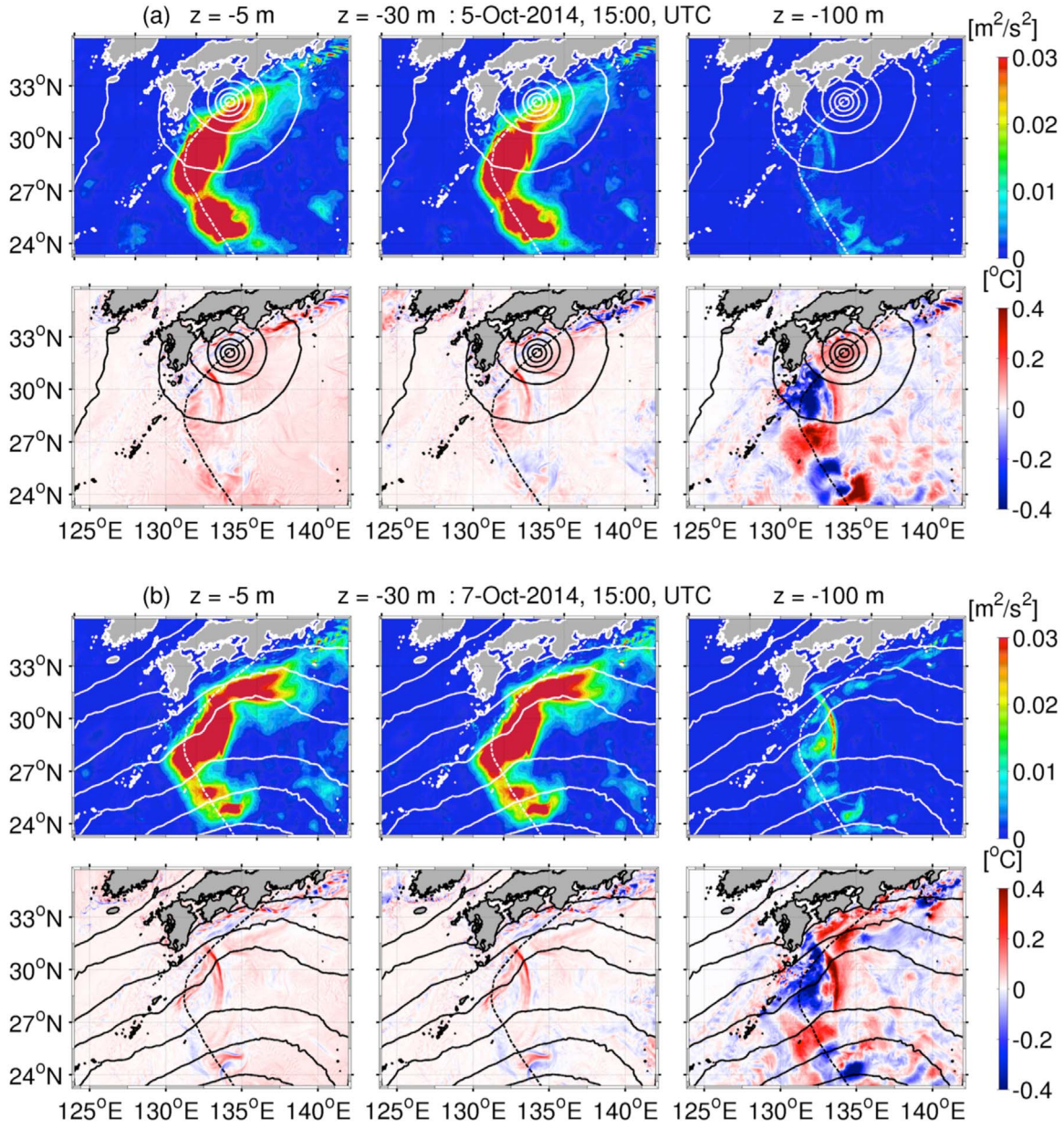

Fig. 4. Snapshots of the (top) eddy kinetic energy (EKE), and (bottom) temperature anomalies in color at the depths of 5, 30 and 100 m, from left to right, (a) on October 5 when Phanfone approached Shikoku Island, and (b) two days later. Both the black and white contours are the sea-level atmospheric pressures (SLPs) from the GPV-MSM. The broken line is the best track of Phanfone.

Kuroshio off the eastern Kyushu Island is readily affected by the typhoons. This is presumably due to the Kuroshio passing by the topography around Cape Ashizuri, which sharpens the Kuroshio front mechanically due to the northward shift of the Kuroshio by the typhoons (Fig. 6). The shift results in the intensified pressure gradient force due jointly to the increased SSH and density gradients that promotes geostrophic zonal acceleration of the Kuroshio and thus stabilizes its path.

5.2. Intrusion of the Kuroshio into the Seto Inland Sea (SIS)

We subsequently analyze the intrusions of the Kuroshio due to the typhoons off the Kii Channel along the KC Line (Fig. 9). The marching typhoons increase the SSH such that the Kuroshio path shifts northward to approach the channel (Fig. 9**a**). The NIOs are initiated prominently in the offshore region after the passages, as visualized in the velocities (Fig. 9**b**-**c**), whereas lower frequency variability at periods of 2–3 days is pronounced in the northern part of the channel associated with counterclockwise circulations shown by bluish colors. The surface relative vorticity normalized by the Coriolis parameter (ranging from 5.66×10^{-5} to $8.58 \times 10^{-5}\,s^{-1}$) fluctuates with the velocity; positive (negative) vorticity is predominant in the north (south) of the Kuroshio (Fig. 9**d**). The typhoons also significantly reduce the temperature of the Kuroshio at lower frequency, more evidently than at the inertial frequency (Fig. 9**e**), in response to the slowly evolving nearshore recurring circulations. In addition, warm water of the Kuroshio occasionally pours into the channel after the typhoons, as visualized by the observed path shown in Fig. 6. These intrusion events are quantified by evaluating the northward heat flux q across the cross section along the MS Line (Fig. 7**b**).

$$q = \int_A \rho C_p u_n T \, dA, \tag{3}$$

where q is the heat flux defined as northward positive, C_p is the specific heat capacity, u_n is the northward velocity normal to the MS Line, and A

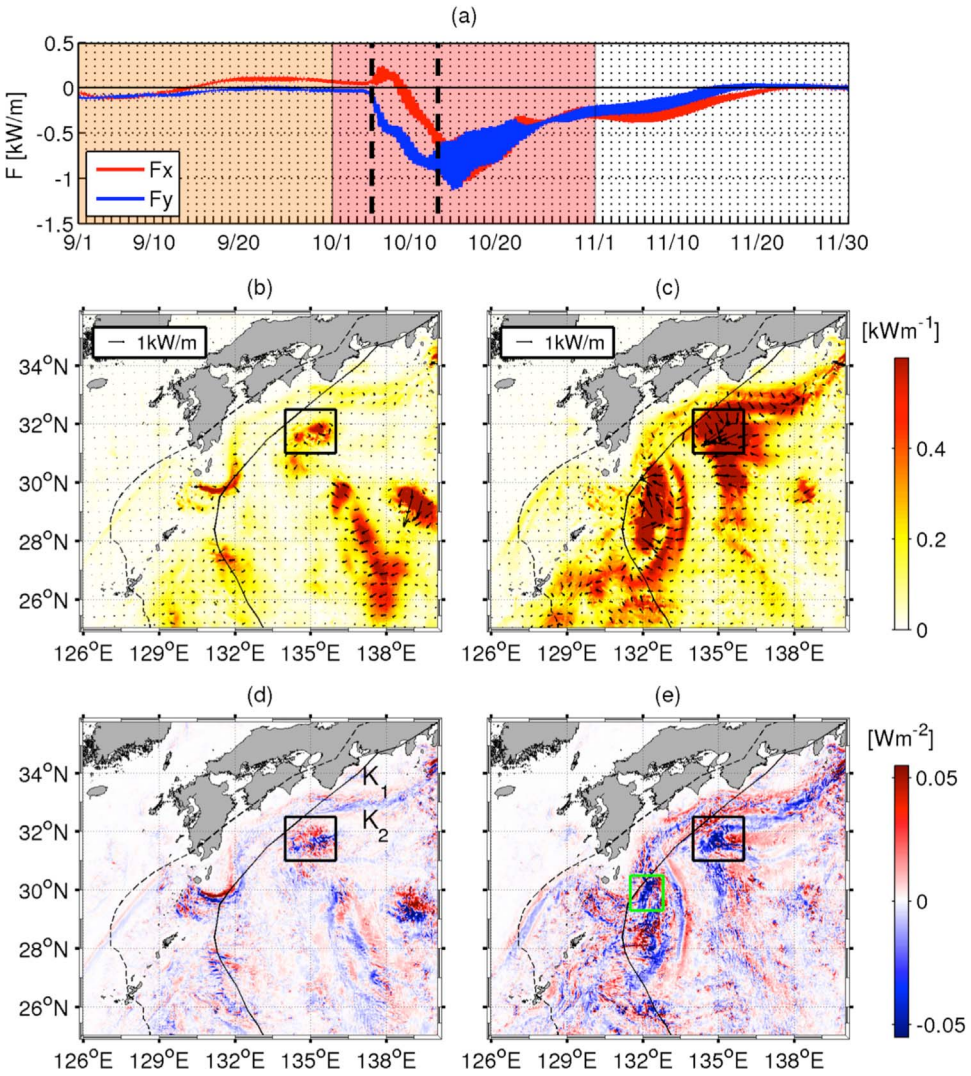

Fig. 5. (a) Time series of the depth-integrated baroclinic energy flux ***F*** from September 1 to November 30, 2014, averaged over the subdomain shown in (b) and (c). The red line is the zonal, eastward (u) component of ***F*** (F_x) and the blue line is the meridional, northward (v) component (F_y). The time-averaged ***F*** vectors are shown in for (b) the non-typhoon period (Sepember 1–30, 2014, orange shade in (a)), and (c) the period that includes the two typhoons (October 1–31, 2014, red shade in (a)) with their magnitude in color. (d)–(e) are the same as (b)–(c), but for the divergence of ***F*** (div ***F***). The bold broken lines in (a) correspond to the times when Phanfone (left) and Vongfong (right) were closest to the analysis area. (For interpretation of the references to color in this figure legend, the reader is referred to the web version of this article.)

is the area of the cross section. We further introduce a decomposition $q = < q > + q''$, where q'' is the eddy (high-frequency) component and $< q >$ is the mean (low-frequency) component with a cut-off period of 30 days. The double prime denotes the fluctuating eddy component for periods shorter than 30 days.

The mean heat flux $< q >$ is negative, which reflects long-term southward flux to the Pacific out of the SIS, consistent with the persistent clockwise circulation formed in the SIS. However, the eddy heat flux q'' predominates over the mean flux and is generally negative with significant temporal variations. Noticeable positive incoming eddy heat flux appears only after the typhoons pass. The variance-preserving power spectrum of q during the typhoon period from September 28 to October 22 has three distinctive peaks at around periods of ~0.5, 1, and 2 days (Fig. 10). The peak at 2 days corresponds to low frequency variability of the counterclockwise circulation in the Kii Channel, north of the MS Line. The intermediate peak at 1 day is the inertial frequency, representing the NIOs. The other peak is in the semi-diurnal period, coinciding with the fluctuations that occur after Vongfong passes

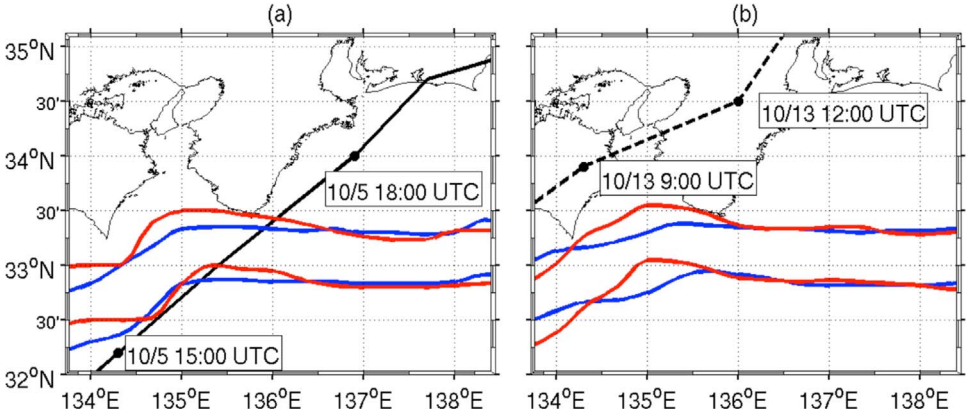

Fig. 6. The Kuroshio paths estimated by the fishery department of the Mie Prefecture before and after (a) Phanfone and (b) Vongfong passed through this area. The area bounded by blue lines indicates the Kuroshio path (a) on October 4 and (b) October 12 before Phanfone and Vonfong respectively. The red lines indicate the Kuroshio path (a) on October 6 and (b) October 14 after the typhoons. The black lines reflect the best tracks of Phanfone (solid) and Vongfong (broken) (For interpretation of the references to color in this figure legend, the reader is referred to the web version of this article.)

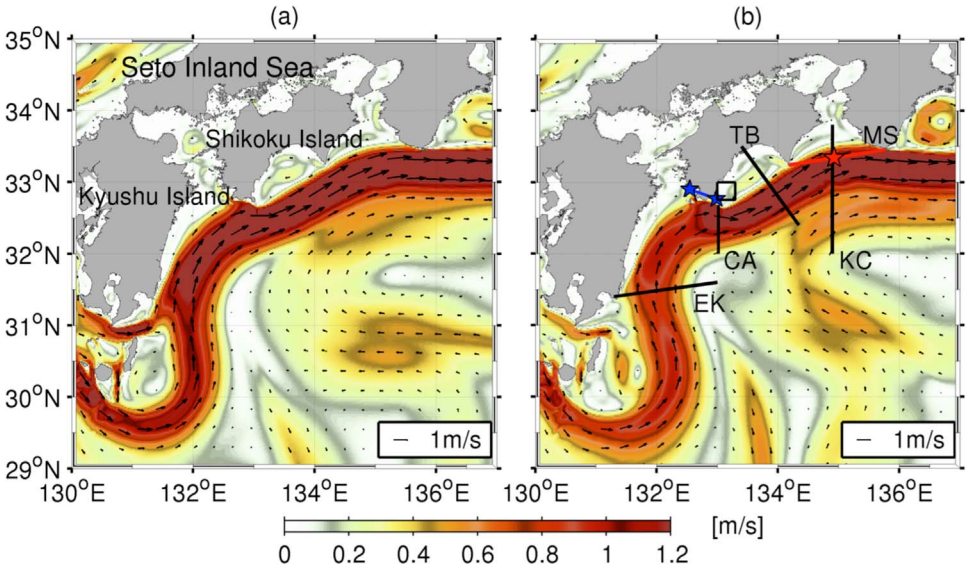

Fig. 7. Monthly-averaged surface velocity vectors for (a) Sepember 2014 and (b) October 2014 and their magnitude in color. In (b), the black lines with the two-letter acronyms indicate the transects, the red line is the cross section for the heat flux analysis (Figs. 9**f** and 10); the blue line is the characteristic length scale for the eddy shedding frequency estimation (Section 6); and the black box represents the subdomain for the computation of the enstrophy, P_eK_e and K_mK_e (Figs. 15 and 16). The acronyms are EK (East coast of Kyushu Island), CA (Cape Ashizuri), TB (Tosa Bay), KC (Kii Channel), and MS (Cape Muroto to Cape Shionomisaki). (For interpretation of the references to color in this figure legend, the reader is referred to the web version of this article.)

(Fig. 9**f**). Perhaps this high-frequency variability reflects higher harmonics of the NIOs because the model does not account for tides, which is usually the prevailing source of the semi-diurnal variability. Note that previous studies (*e.g.*, Isobe et al., 2010) have reported that intrusions of the Kuroshio warm water occur at the Bungo Channel and Kii Channel due to the fluctuations of the Kuroshio path.

5.3. Impacts on the SIS circulation

To quantify the influences of the two typhoons on the circulation in the SIS, time series of the volume fluxes across the 12 transects (Fig. 1**c**) are plotted in Fig. 11. Overall, weak, positive, and clockwise transport is predominant throughout the SIS, except for the periods of the two typhoons. Both the typhoons abruptly make the sign of the fluxes negative, leading to intensified counterclockwise circulations. Extensive negative fluxes are observed in particular near the Kii (L) and Bungo (A) channels, followed by moderate positive fluxes as aftershocks. This suggests that the meridional (northward) transition of the Kuroshio path due to the typhoons (Figs. 6 and 9**a**) influences the intermittent directional inversion of the mean clockwise circulation in the SIS, which provokes the intrusion at the Kii Channel and discharge out of at the Bungo Channel. The negative fluxes in the SIS are not only affected by the typhoon-induced inverse circulations but also by counter-clockwise wind stress associated with the approaching Phanfone (not shown) and Vongfong (Fig. 12), particularly at the transects far from the two channels. Note that Vongfong induces more negative fluxes because its track is closer to the SIS (Fig. 1**b**) and its wind stress is more intense than that of Phanfone. The averaged volume flux in the SIS is ~0.01 Sv ($1 \times 10^4\ m^3\ s^{-1}$) in the clockwise direction under normal, non-typhoon conditions, whereas the typhoons alter it to approximately −0.08 Sv in the opposite direction. Because 0.08 Sv is ~130 times as much as the sum of the mean discharges from all major rivers pouring into the SIS, the typhoons are anticipated to influence the estuarine environment.

To quantitatively measure the influence of the typhoons on the SIS environment, we evaluate a water exchange time scale T_e expressed as:

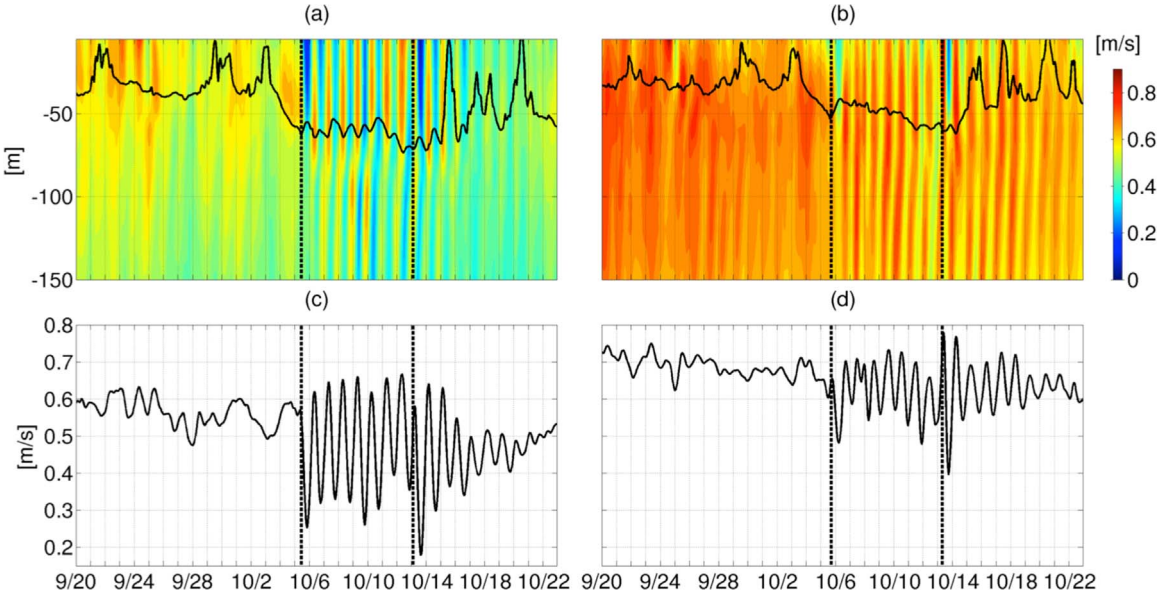

Fig. 8. (a) and (b) Hovmöller diagrams of the streamwise northward velocity as a function of time and depth averaged over the EK Line (left column; Fig. 7**b**) and the TB Line (right column) with the mixed layer depth estimated from the KPP model (black line); (c) and (d) depth-averaged velocity of (a) and (b) down to 80-m depth. The bold broken lines in (c) and (d) represent the times when Phanfone (left lines) and Vongfong (right lines) were closest to the transects.

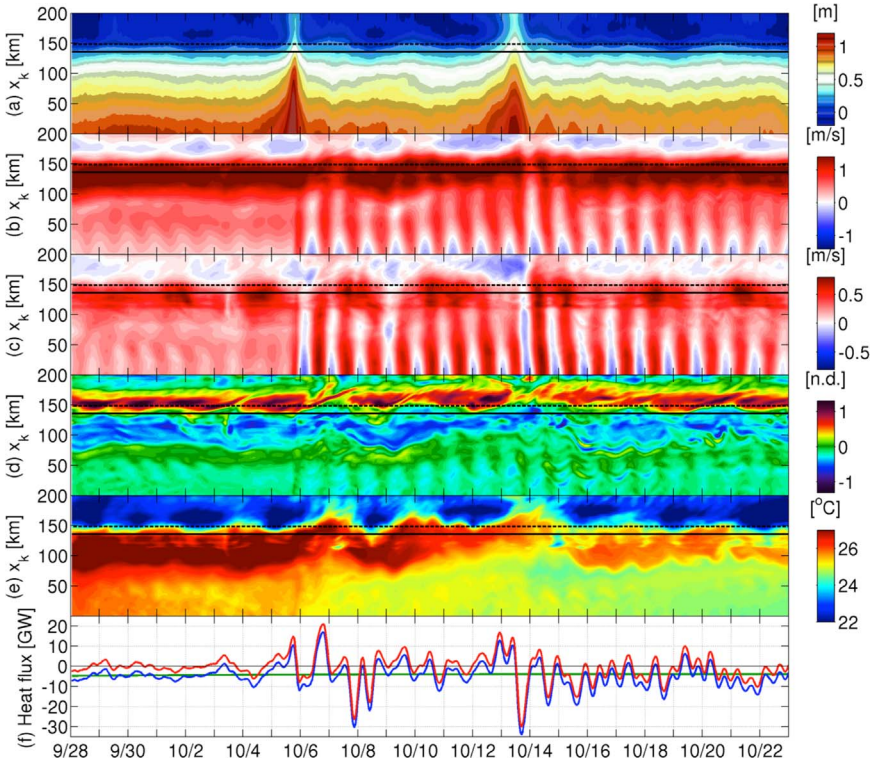

Fig. 9. Hovmöller diagrams of (a) SSH, (b) transverse southward and (c) streamwise eastward velocities at 50-m depth, (d) normalized relative vorticity at the surface, and (e) surface potential temperature along the KC Line (Fig. 7**b**). The ordinate is the northward distance x_k measured from the offshore end of the KC Line, while the abscissa is the date in 2014. (f) Time series of the heat fluxes q (blue line) at the MS Line, where the red line is its high-frequency component q'' and the green line is the mean heat flux $< q >$. The black solid lines in (a)–(e) are the time-averaged Kuroshio axis from September 20 to October 22, 2014, evaluated according to the JMA definition, where the maximum current occurs at 50-m depth, while the broken lines are the location of the MS Line crossing the KC Line. (For interpretation of the references to color in this figure legend, the reader is referred to the web version of this article.)

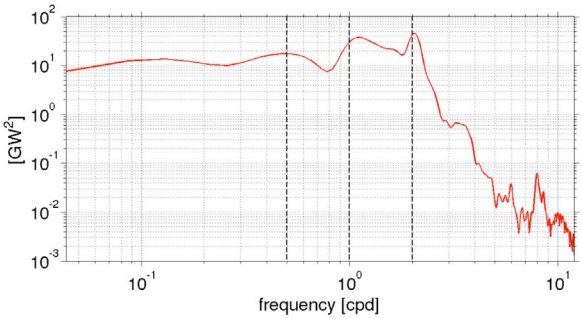

Fig. 10. Variance-preserving frequency spectrum of heat flux q across the MS Line located at the entrance of the Kii Channel. The broken lines indicate the spectral peak periods around 2, 1 (near-inertial period), and 0.5 days (semi-diurnal period), from right to left.

$$T_e = V / \sum_k F_k \quad , \tag{4}$$

where V is the volume of the segment (a – i; see Fig. 1**c**) and F_k is the outgoing volume flux ($m^3 s^{-1}$) from the segment through the surrounding transect k. The maximum F_k is used for the typhoon periods, whereas the monthly averaged F_k for September 2014 is applied for the non-typhoon period. As summarized in Table 2, both typhoons significantly reduce the exchange time scale T_e of all the segments compared with those for the non-typhoon period. Even for the segments far from the two channels, T_e reduces to ~30% of that under the normal conditions. In other words, the water exchange in the SIS is considerably enhanced by the typhoons (~3–20 times), resulting in the potential impact on the estuarine environment.

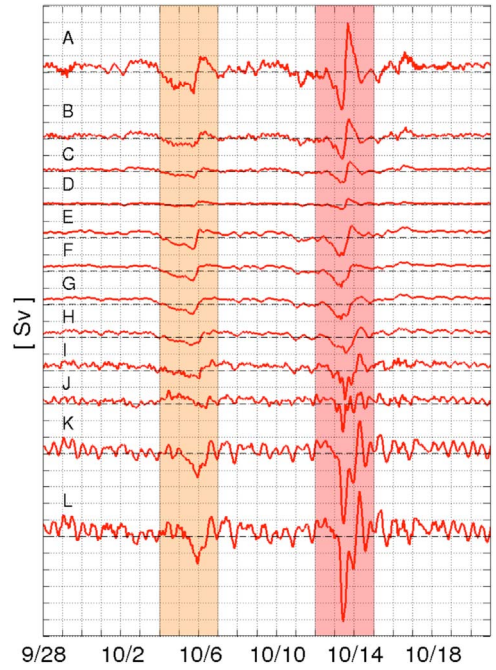

Fig. 11. Time series of volume fluxes in the SIS across the 12 transects A–L plotted in Fig. 1**c**. The clockwise transport flowing from L (west, at the Bungo Channel) to A (east, at the Kii Channel) is defined as positive. One scale in the ordinate is 0.05 Sv. The shaded areas represent approximate periods during Phanfone (orange) and during Vongfong (red). (For interpretation of the references to color in this figure legend, the reader is referred to the web version of this article.)

6. Typhoon-Kuroshio-eddy interaction

6.1. Topographic eddy shedding

To assess the typhoon-induced oscillations of the Kuroshio path that occurred off Shikoku Island, we conduct rotary spectral analysis on the horizontal velocities at 50-m depth, where the Kuroshio normally has its maximum velocity, along the TB Line off Tosa Bay, the upstream region of the Kii Channel (Fig. 13). Although the low frequency variability is apparent, a distinct peak appears around the near-inertial frequency in the clockwise-rotating components due to the NIOs on the offshore side of the Kuroshio path, as indicated by the dotted ellipse near P_1. On the coastal side, it peaks at periods of ~3 days with

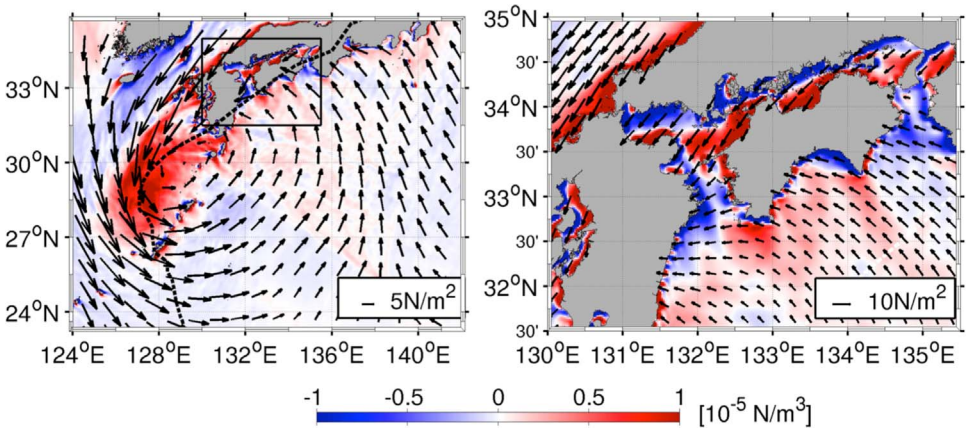

Fig. 12. Wind stress vectors and their curl in color, averaged for October 12–13 when Vongfong approached the SIS. The right panel is the blow-up of the entire model domain on the left.

Table 2
Water exchange time scale T_e in days represented by Eq. (4) for the nine segments of the SIS ($a-i$, Fig. 1**c**) during Phanfone and Vongfong and for the non-typhoon, normal period (September 2014).

Segment	Non-typhoon	Phanfone	Vongfong
a	552	219	105
b	767	897	554
c	1260	303	184
d	124	69	41
e	122	60	39
f	271	199	93
g	418	249	73
h	1556	272	84
i	1696	274	88

counterclockwise rotation, denoted by P_2.

To examine the possible mechanism responsible for the ~3 day peak period, sequential plots of the fluctuating component of the normalized relative vorticity at the surface are depicted in Fig. 14, where the slow components for periods longer than 30 days are subtracted as the background vorticity mainly due to the Kuroshio. On October 6, just after Phanfone passed, a pair of positive and negative vorticity shed at Cape Ashizuri, subsequently rolling up into circular coherent eddies. These eddies then partly accumulate in Tosa Bay but mostly propagate eastward to the Kii Channel. The eddy-shedding period is ~3 days long, corresponding to the low frequency velocity spectral peak at Tosa Bay (P_2 in Fig. 13). As a side remark, although the period of the studies is different, such a ~3 day eddy-shedding period was detected in the Kii Channel through an ADCP measurement (Uchiyama et al., 2016).

6.2. Eddy shedding frequency

Such an eddy shedding frequency might roughly be confirmed based on Strouhal number. For instance, the universal Strouhal number S_t defined in Bearman (1967) has occasionally been used for oscillating motions in geophysical fluids, such as Kármán vortex streets behind islands:

$$S_t = fH/U \cong 0.181, \tag{5}$$

where f is an oscillation frequency, U is the characteristic velocity, and H is the characteristic length scale. Eq. (5) is known to be valid for a wide range of Reynolds numbers. A similar result in a form of S_t (~0.18) is derived from a linear stability analysis of shear turbulence (*e.g.*, Schar and Smith, 1993). If we assume that $U = 1.0\ \mathrm{ms}^{-1}$, based on the mean Kuroshio, is the velocity, and $H = 50$ km, based on the lateral length of Cape Ashizuri (blue line in Fig. 7**b**), is the effective thickness of the shear layer, then we obtain $f = 0.311$ cpd (*i.e.*, a period of 3.22 days), consistent with the spectral peak frequency near P_2 in Fig. 13. Therefore, topographically generated mesoscale eddies shed from Cape Ashizuri are the plausible main cause of the low frequency velocity variability.

The estimated eddy-shedding period of ~3 days is further ensured quantitatively using a surface enstrophy time series on the downstream side of Cape Ashizuri (Fig. 15**a**). The enstrophy of the positive and negative relative vorticity components at the surface is evaluated separately to determine the prevailing rotation in Tosa Bay. Although the negative component is prominent before Phanfone passes on October 5, the positive component significantly intensifies with temporal fluctuations at a period of several days after the passage. The variance-preserving frequency spectra for the positive and negative enstrophy components peak at ~3 days, particularly for the positive vorticity component (Fig. 16). Therefore, the typhoons considerably promote counterclockwise, cyclonic eddies shed from Cape Ashizuri, leading to ~3-day period velocity fluctuations in Tosa Bay. We should note that, whereas Fig. 15**a** shows smaller enstrophy fluctuations after Vongfong (*i.e.*, after Oct. 13) than Phanfone, it is mostly due to our choice of the

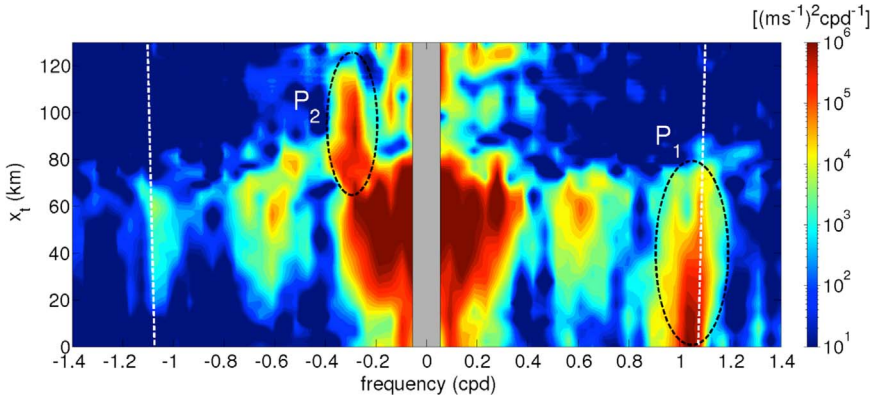

Fig. 13. Velocity rotary spectrum for September 28 to October 22 along the TB Line (Fig. 1**c**) at $z = -50$ m, showing the clockwise (right) and counterclockwise (left) components. The ordinate is the shoreward distance measured from the southern end of the TB Line, while the abscissa is the frequency in cycles per day (cpd). The white broken lines are the corresponding inertial frequency. The gray area corresponds to undetectable lower frequencies.

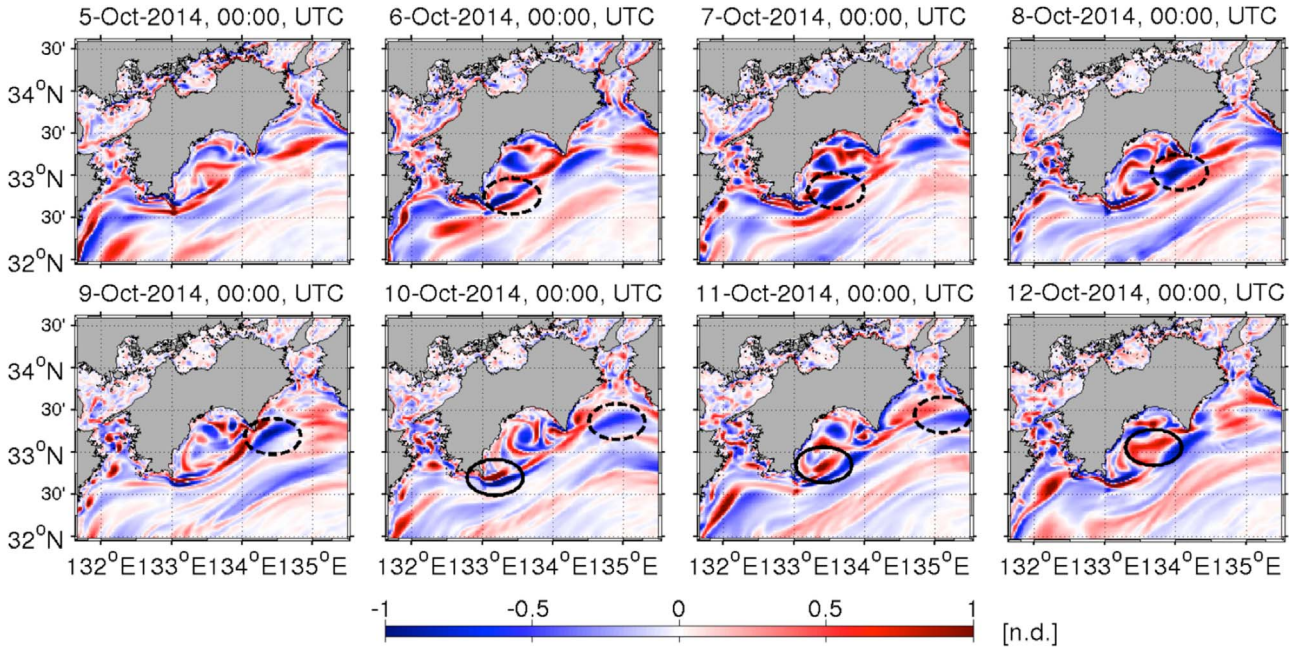

Fig. 14. Temporal evolution of the normalized vorticity anomaly at the surface for October 5–12, 2014 off Shikoku Island. The vorticity anomaly is evaluated from the eddy component of lateral velocity for the periods shorter than 30 days to exclude the background vorticity in the slowly evolving transient Kuroshio. The black broken circles are shown to track the negative vorticity anomaly, whereas the black circles reflect the positive vorticity anomaly.

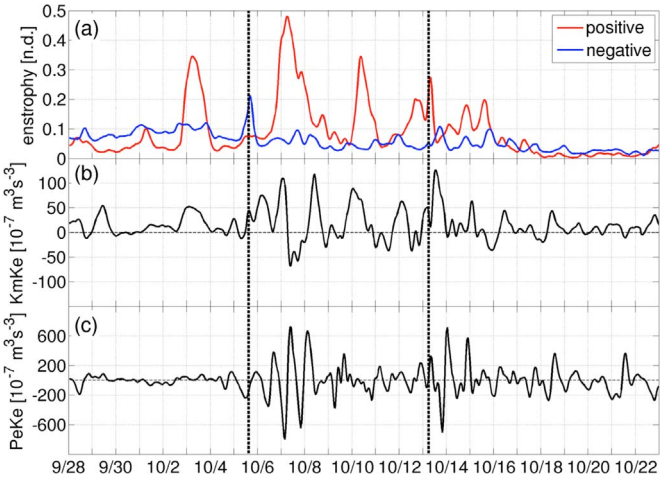

Fig. 15. Time series of (a) enstrophy of the normalized relative vorticities at the surface for positive (cyclonic, red) and negative (anti-cyclonic, blue) components; (b) barotropic conversion rate, K_mK_e (Eq. (6)); and (c) baroclinic conversion rate, P_eK_e (Eq. (7)). All variables are averaged over the rectangular area on the east of Cape Ashizuri shown by the black box in Fig. 7**b**. The K_mK_e and P_eK_e values are integrated vertically down to 200-m depth. (For interpretation of the references to color in this figure legend, the reader is referred to the web version of this article.)

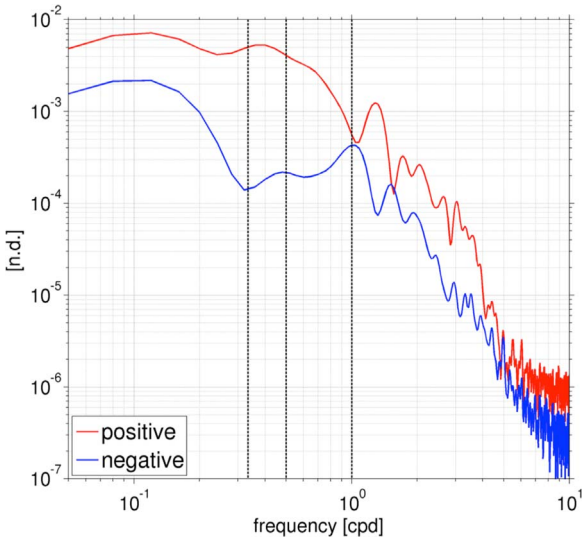

Fig. 16. Variance-preserving frequency spectra of enstrophy from September 28 to October 22 for the positive (red) and negative (blue) components shown in Fig. 15**a**. The broken lines are the periods of 1, 2, and 3 day, from right to left. (For interpretation of the references to color in this figure legend, the reader is referred to the web version of this article.)

analysis subdomain (black box in Fig. 7**b**). As seen in the Fig. 9**d**, eddies associated with Vongfong fluctuate as intensively as those with Phanfone along the KC line.

6.3. Eddy generation mechanism

The energy conversion rates in the eddy kinetic energy (K_e) conservation equation quantify the relative importance of instability and eddy-mean interaction mechanisms (*e.g.*, Marchesiello et al., 2003; Dong et al., 2006; Klein et al., 2008; Uchiyama et al., 2017a). To better understand the mechanism of the eddy generation and resultant intensification of enstrophy, we focus on the two leading terms that account for the conversion of the mean kinetic energy to eddy kinetic energy, K_mK_e (*viz.,* barotropic conversion rate), and the conversion of eddy potential energy to eddy kinetic energy, P_eK_e (*viz.,* baroclinic conversion rate).

$$K_mK_e = -\left(\overline{u''^2}\frac{\partial \bar{u}}{\partial x} + \overline{u''v''}\frac{\partial \bar{u}}{\partial y} + \overline{u''w''}\frac{\partial \bar{u}}{\partial z} + \overline{u''v''}\frac{\partial \bar{v}}{\partial x} + \overline{v''^2}\frac{\partial \bar{v}}{\partial y} + \overline{v''w''}\frac{\partial \bar{v}}{\partial z}\right), \tag{6}$$

$$P_eK_e = -\frac{g}{\rho_0}\overline{\rho''w''}, \tag{7}$$

where (x, y, z) are the horizontal and vertical coordinates; w is the vertical velocity; ρ_0 (1027.5 kg m^{-3}) is the Boussinesq reference density; the overbar is an ensemble-averaging operator; and the double

prime denotes the fluctuating eddy component for periods shorter than 30 days. A positive K_mK_e implies the extraction of K_e from the mean kinetic energy to generate eddies by shear instability. Likewise, if P_eK_e is positive, baroclinic instability is expected to produce K_e.

Fig. 15**b**-**c** illustrate the time series of K_mK_e and P_eK_e integrated vertically down to a 200-m depth and averaged over the same subdomain as the enstrophy in Fig. 15**a**. Intensification of the positive K_mK_e occurs after the typhoons passed coincidently with the increase of enstrophy. They are slightly out of phase, whereas the increase of the positive K_mK_e corresponds to the increase of the temporal change in enstrophy. The positive K_mK_e lasts over a relatively long period after Phanfone passes, similarly to the enstrophy intensification. In contrast, P_eK_e fluctuates around zero with periodic largely positive and negative values alternatively appearing with less notable synchronicity with the enstrophy variations. In summary, the enstrophy amplification on the eastern side of Cape Ashizuri is mainly promoted by the shear instability due to topographic eddy shedding with a characteristic frequency of ~3 days approximated by the universal Strouhal number, while the baroclinic instability associated with the sharpening of the Kuroshio SST front (not shown) plays a secondary role.

6.4. Typhoon-Kuroshio-eddy interaction

Fig. 17 shows the time series of the location, streamwise velocity, and prevailing direction of the Kuroshio axis at the three transects off Cape Ashizuri (CA Line; Fig. 7**b**), Tosa Bay (TB Line), and the Kii Channel (KC Line) to examine how the typhoons modify the Kuroshio and its path. Here, the Kuroshio axis is determined as the streamline at 50-m depth that connects the lateral locations of the Kuroshio core, where the maximum velocity occurs, according to the definition of JMA. At Cape Ashizuri, the axis is shifted northward (shaded in red) by ~10 km after the passages of the two typhoons (Fig. 17**a**). As shown in Fig. 15, a prominent increase of K_mK_e and resultant enstrophy amplification take place concurrently with these northward shifts. Upon the arrival of Phanfone on October 5, the velocity starts to oscillate and to decelerate at ~0.2 ms^{-1}. The direction is also modified to rotate the axis clockwise to 30° with the typhoon passages at 6:00 on October 7. Thus, the typhoons push the Kuroshio path northward to close to the coastal topography, leading to the deceleration and clockwise turn of the axis. Likewise, at Tosa Bay, the axis moves northward at the passages, whereas it reverts back southward shortly after (Fig. 17**b**). In contrast, a direction change occurs in the counterclockwise direction that turns the axis to the north, indicating the intrusion of the Kuroshio into the bay.

Northward axis meanders of up to 15 km appear in the Kii Channel (KC Line) as a result of the typhoon-induced shift (Fig. 17**c**). The velocity deceleration is also evident, particularly with Vongfong approaching on October 13; the velocity gradually recovers in ~5 days. Similarly to the TB Line, topographically generated eddies shed from Cape Ashizuri propagate eastward to the Kii Channel (Fig. 14) to provoke the oscillation of the Kuroshio at the CA line. It is worth noting that the axis direction oscillates with an amplitude of ~10° without the typhoons, whereas it increases to ~25° when the two typhoons pass with distinctive periodicity at the period of ~3 days. On the contrary, the oscillating periods at the CA and TB lines are dominated by the period of ~1 day, the near-inertial period. These results suggest that the combination of NIOs and eddies shedding from the two capes jointly promotes the fluctuations of the Kuroshio axis.

We then investigate the spatiotemporal fluctuations of the Kuroshio path due to the typhoons at depths down to 500 m in the frequency space. Analogously to the definition of the Kuroshio axis, the locations of the Kuroshio path at an arbitrary depth is determined as the horizontal coordinate at which the maximum velocity occurs at that depth along the transect. The two transects, one is off the east coast of Kyushu Island (EK Line) and the other is off Tosa Bay (TB Line), are examined using the frequency spectra of the locations of the Kuroshio path as a function of depths down to 500 m deep (Fig. 18). At the EK Line, the spectrum is significantly intensified in the upper ocean from the surface down to ~150 m with a considerable downward decrease (Fig. 18**a**). Because a peak appears at the inertial frequency (broken lines in Fig. 18), the NIOs are the predominant factors inducing the fluctuations of the Kuroshio path. Another peak at very low frequencies (periods of longer than 5 days) is apparent, whereas it is also confined in the upper ocean. In turn, the peak around the inertial frequency is much smaller at the TB Line, except for depth deeper than 400 m, above which the Kuroshio main body exists (Fig. 18**b**). The spectral energy at the TB Line is much smaller than that at the EK Line, which is consistent with the more stable path off Shikoku Island compared with that off Kyushu Island (Section 5). The most notable peak appears at around the period of 3 days at all depths at the TB Line as a consequence of the topographic eddy-shedding.

In summary, the "typhoon-Kuroshio-eddy interaction", according to the sequence of their occurrence, took place off Shikoku Island. This process differs conceptually and phenomenologically from the "typhoon-eddy-Kuroshio interaction" reported by Sun et al. (2009), where collisions of eddies intensified by a typhoon initiated a meander of the

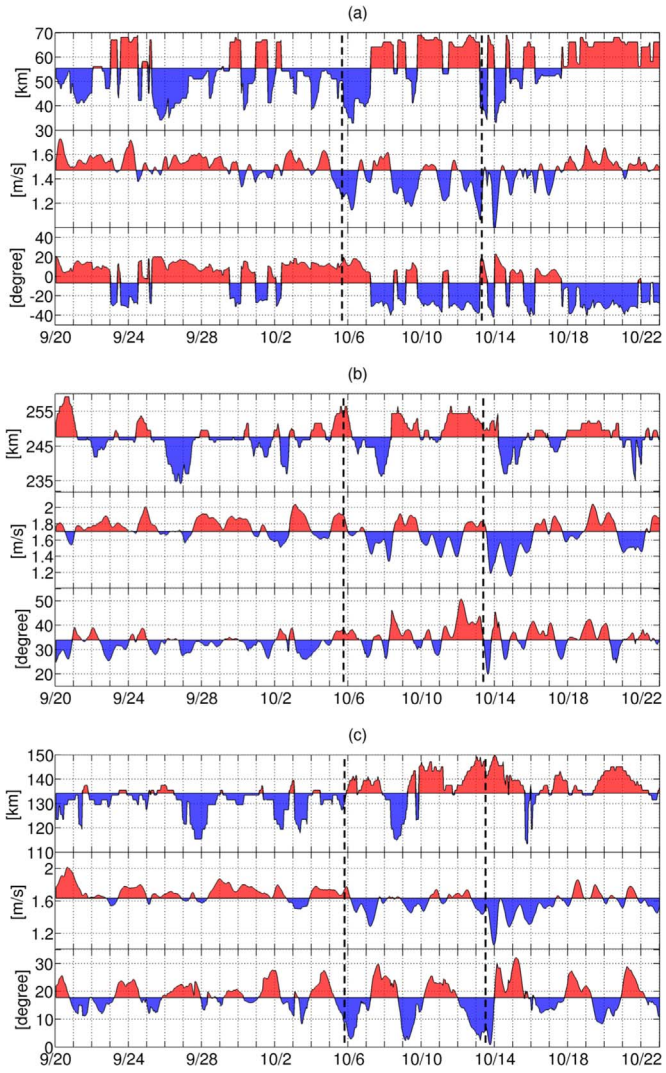

Fig. 17. Time series of the shoreward distance from the southern end of the transect to the Kuroshio axis (top), the maximum velocity of the Kuroshio at 50-m depth (middle), and the corresponding counterclockwise angle of the flow direction measured from the east (bottom) at (a) CA (Cape Ashizuri) Line, (b) TB (Tosa Bay) Line, and (c) KC (Kii Channel) Line. The red (blue) shaded areas exhibit greater (smaller) values than the time averages. (For interpretation of the references to color in this figure legend, the reader is referred to the web version of this article.)

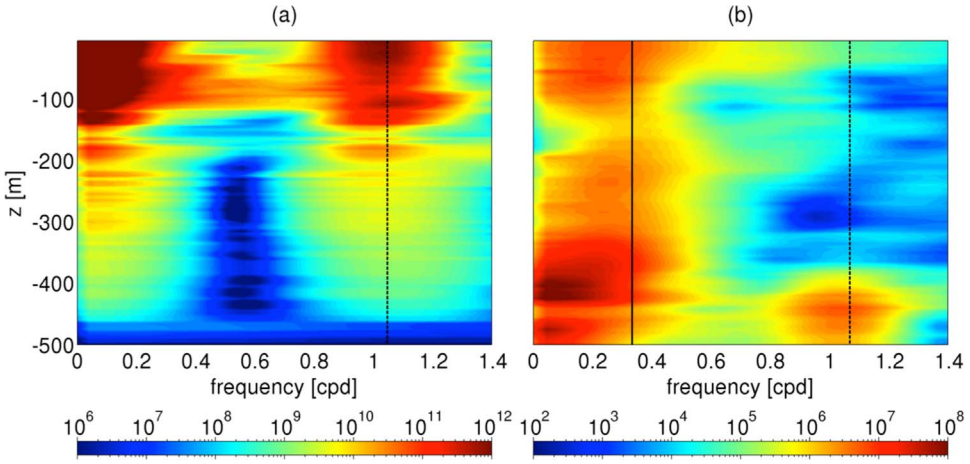

Fig. 18. Power spectral density (m^2cpd^{-1}) of the along-transect locations of the Kuroshio core analyzed for October 1–22 as a function of depth (a) off the eastern Kyushu Island (EK Line; Fig. 7**b**) and (b) off Tosa Bay (TB Line; Fig. 7**b**). The Kuroshio core is determined at each depth where the maximum streamwise Kuroshio velocity takes place. The broken lines indicate the inertial frequency along the transects. The solid line in (b) shows the approximate eddy-shedding period of 3 days. Notice that different color scales are used.

Kuroshio. In contrast, the present interaction mechanism is initiated by the northward shift of the Kuroshio axis due to the two consecutive typhoons, which results in topographic eddy shedding. Both the interactions are anticipated to be crucial in modifying the Kuroshio, and thus have potential impacts on nearshore dynamics and associated coastal environment.

7. Conclusions

We investigate the impact of two consecutive super typhoons that occurred in the fall of 2014 on the Kuroshio and adjacent coastal waters in the northwestern Pacific using high-resolution, retrospective ROMS modeling. The modeling framework is configured based on a one-way offline nesting technique that enables the downscaling of the assimilative JCOPE2 oceanic reanalysis with a realistic atmospheric forcing based on the assimilative GPV-MSM reanalysis products. A model-data comparison is conducted to confirm that the present model reasonably well reproduces the Kuroshio and 3D oceanic structure on the Pacific side of Japan.

The two typhoons prominently generate near-inertial motions, particularly on the right side of the typhoon tracks. The near-inertial internal waves (NIIWs) are induced in the thermocline at ~100-m depth. These NIIWs are extensively energized by ~1 kW m^{-1} near the Kuroshio off the Shikoku and Kyushu islands, which is considered to be quite significant because it is equivalent to half of the energy flux of internal tides. Furthermore, the NIIWs interact with the Kuroshio and cause its path to fluctuate off the east coast of Kyushu Island (EK Line, Fig. 7**b**) and off Tosa Bay (TB Line, Fig. 7**b**), where the NIIWs are most energetic. However, the fluctuations of the path are substantially suppressed at the TB Line because of the northward shift of the path due to the typhoons that decelerate the flow rate and stabilize the path. The near-inertial oscillations (NIOs) are also intensified in the mixed layer, which promote periodic changes in the velocity and direction of the Kuroshio axis. The two super typhoons cause the considerable deceleration of the streamwise velocity of the Kuroshio at 0.2–0.3 ms^{-1} on average. This deceleration occurs as a part of the NIOs, and thus the velocity and direction of the Kuroshio axis are instantaneously and largely altered at the period of ~1 day.

In addition to the generation of such high-frequency, near-inertial variability, the Kuroshio off Shikoku Island evidently shifts northward with the typhoons, leading to the quasi-persistent deceleration and change in the mean direction of the Kuroshio axis that lasts for several days after the passages. This northward shift enhances the interactions between the Kuroshio and topography and promotes eddy shedding from Cape Ashizuri. The shedding period is estimated to be ~3 days based on the universal Strouhal number (Bearman, 1967), which is consistent with the peak period in the counterclockwise component of the velocity rotary spectrum. We thus call this process as the "typhoon-Kuroshio-eddy interaction", which differs from the typhoon effects on the Kuroshio studied in Sun et al. (2009). The enstrophy of the associated counterclockwise eddies with positive relative vorticity is apparently excited after the typhoon passes with a fluctuating period of ~3 days. The energy conversion analysis reveals that the positive barotropic conversion K_mK_e synchronously arises with the positive enstrophy, whereas the baroclinic conversion P_eK_e is of secondary importance. Hence, the shear instability associated with the topographic eddy generation is the key mechanism responsible for the sub-inertial oscillations.

The near-inertial dynamics and sub-inertial eddy shedding concurrently affect the Kuroshio path and alter its axis at fluctuating periods of ~1 day and ~3 days. The typhoons lead to a significant change in the Kuroshio axis, which mostly turns into counterclockwise direction to promote northward flow near the coast. Indeed, the pronounced intrusions into the Seto Inland Sea (SIS) occur at the Kii Channel after the typhoons pass. The SIS has a persistent clockwise (eastward) circulation of ~0.01 Sv under the non-typhoon conditions, whereas the intrusions abruptly promote counterclockwise (westward) circulation of ~0.08 Sv, resulting in inversed circulations that remarkably intensify the water exchange rate in many of the segments of the SIS.

Acknowledgements

This research was supported by the JSPS Grant-in-Aid for Scientific Research (Grant Numbers: 15H00977, 15H04049, and 15KK0207) and the JST-CREST program (Grant Number: JPMJCR12A6).

References

Akitomo, K., Awaji, T., Imasato, N., 1991. Kuroshio path variation south of Japan. 1. Barotropic inflow-outflow model. J. Geophys. Res. 96, 2549–2560. http://dx.doi.org/10.1029/90JC02030.

Akitomo, K., Kurogi, M., 2001. Path transition of the Kuroshio due to mesoscale eddied: a two-layer, wind-driven experiment. J. Oceanogr. 57, 735–741. http://dx.doi.org/10.1023/A:1021292627245.

Bearman, P.W., 1967. On vortex street wakes. J. Fluid Mech. 28, 625–641. http://dx.doi.org/10.1017/S0022112067002368.

Becker, J.J., Sandwell, D.T., Smith, W.H.F., Braud, J., Binder, B., Depner, J., Fabre, D., Factor, J., Ingalls, S., Kim, S.-H., Ladner, R., Marks, K., Nelson, S., Pharaoh, A., Trimmer, R., Von Rosenberg, J., Wallace, G., Weatherall, P., 2009. Global bathymetry and elevation data at 30 arc seconds resolution: SRTM30_PLUS. Mar. Geodsy 32 (4), 355–371. http://dx.doi.org/10.1080/01490410903297766.

Buijsman, M., Uchiyama, Y., McWilliams, J.C., Hill-Lindsay, C.R., 2012. Modeling semidiurnal internal tides in the Sourthern California Bight. J. Phys. Oceanogr. 42, 62–77. http://dx.doi.org/10.1175/2011JPO4597.1.

Church, J.A., Joyce, T.M., Price, J.F., 1989. Current and density observations across the wake of Hurricane Gay. J. Phys. Oceanogr. 19, 259–265. http://dx.doi.org/10.1175/1520-0485(1989)019<0259:CADOAT>2.0.CO;2.

Dong, C., McWilliams, J.C., Shchepetkin, A.F., 2006. Island wakes in deep water. J. Phys. Oceanogr. 37, 962–981. http://dx.doi.org/10.1175/JPO3047.1.

Durski, S.M., Glenn, S.M., Haidvogel, D.B., 2004. Vertical mixing schemes in the coastal ocean: Comparison of the level 2.5 Mellor-Yamada scheme with an enhanced version of the K profile parameterization. J. Geophys. Res. 109, C01015. http://dx.doi.org/10.1029/2002JC001702.

Glenn, S.M., Miles, T.N., Seroka, G.N., Xu, Y., Forney, R.K., Yu, F., Roarty, H., Schofield, O., Kohut, J., 2016. Stratified coastal ocean interactions with tropical cyclones. Nat. Comm. 7, 10887. http://dx.doi.org/10.1038/ncomms10887.

Hodur, R.M., 1997. The naval research laboratory's Coupled Ocean/Atmosphere Mesoscale Prediction System (COAMPS). Mon. Weather Rev. 125, 1414–1430. http://dx.doi.org/10.1175/1520-0493(1997)125<1414:TNRLSC>2.0.CO;2.

Imawaki, S., Uchida, H., Ichikawa, H., Fukasawa, M., Umatani, S., the ASUKA Group, 2001. Satellite altimeter monitoring the Kuroshio transport south of Japan. Geophys. Res. Lett. 28, 17–20. http://dx.doi.org/10.1029/2000GL011796.

Isobe, A., Guo, X., Takeoka, H., 2010. Hindcast and predictability of sporadic Kuroshio-water intrusion (kyucho of the Bungo Channel) into the shelf and coastal waters. J. Geophys. Res. 115, C04023. http://dx.doi.org/10.1029/2009JC005818.

Isoguchi, O., Shimada, M., Kawamura, H., 2010. Characteristics of ocean surface winds in the lee of an isolated island observed by synthetic aperture radar. Mon. Weather Rev. 139, 1744–1761. http://dx.doi.org/10.1175/2010MWR3564.1.

Kamidaira, Y., Uchiyama, Y., Kawamura, H., Kobayashi, T., Furuno, A., 2018. Submesoscale mixing on initial dilution of the radionuclides released from the Fukushima Dai-ichi Nuclear Power Plant. J. Geophys. Res. Oceans.

Kang, D., Fringer, O.B., 2012. Energetics of barotropic and baroclinic tides in the Monterey Bay area. J. Phys. Oceanogr. 42, 272–290. http://dx.doi.org/10.1175/JPO-D-11-039.1.

Kawabe, M., 1985. Sea level variations at the Izu islands and typical stable paths of the Kuroshio. J. Oceanogr. Soc. Jpn. 41, 307–326. http://dx.doi.org/10.1007/BF02109238.

Kawabe, M., 1995. Variations of current path, velocity, and volume transport of the Kuroshio in relation with the large meander. J. Phys. Oceanogr. 25, 3103–3117. http://dx.doi.org/10.1175/1520-0485(1995)025<3103:VOCPVA>2.0.CO;2.

Klein, P., Hua, B.-L., Lapeyre, G., Capet, X., Le Gentil, S., Sasaki, H., 2008. Upper ocean turbulence from high-resolution 3D simulations. J. Phys. Oceanogr. 38, 1748–1763. http://dx.doi.org/10.1175/2007JPO3773.1.

Kumar, N., Feddersen, F., Uchiyama, Y., McWilliams, J., O'Reilly, W., 2015. Mid-shelf to surf zone coupled ROMS-SWAN model-data comparison of waves, currents, and temperature Diagnosis of subtidal forcing and response. J. Phys. Oceanogr. 45, 1464–1490. http://dx.doi.org/10.1175/JPO-D-14-0151.1.

Kumar, N., Feddersen, F., Suanda, S., Uchiyama, Y., McWilliams, J., O'Reilly, W., 2016. Mid- to inner-shelf coupled ROMS-SWAN model-data comparison of currents, and temperature: Diurnal and semi-diurnal variability. J. Phys. Oceanogr. 46, 841–862. http://dx.doi.org/10.1175/JPO-D-15-0103.1.

Large, W.G., Mcwilliams, J.C., Doney, S., 1994. Oceanic vertical mixing: A review and a model with a nonlocal boundary-layer parameterization. Rev. Geophys. 32, 363–403. http://dx.doi.org/10.1029/94RG01872.

Nakamura, H., Yamashiro, T., Nishina, A., Ichikawa, H., 2006. Time-frequency variability of Kuroshio meanders in Tokara Strait. Geophys. Res. Lett. 33, L21605. http://dx.doi.org/10.1029/2006GL027516.

Nakata, H., Funakoshi, S., Nakamura, M., 2000. Alternating dominance of postlarval sardine and anchovy caught by coastal fishery in relation to the Kuroshio meander in the Enshu-nada Sea. Fish. Oceanogr. 9, 248–258. http://dx.doi.org/10.1046/j.1365-2419.2000.00140.x.

Nash, J.D., Alford, M.H., Kunze, E., 2005. Estimating internal wave energy fluxes in the ocean. J. Atmos. Ocean. Technol. 22, 1551–1570. http://dx.doi.org/10.1175/JTECH1784.1.

Marchesiello, P., Benshila, R., Almar, R., Uchiyama, Y., McWilliams, J., Shchepetkin, A., 2015. On tridimensional rip current modeling. Ocean Modell. 96 (1), 36–48. http://dx.doi.org/10.1016/j.ocemod.2015.07.003.

Mason, E., Molemaker, J., Shchepetkin, A.F., Colas, F., McWilliams, J.C., Sangrà, P., 2010. Procedures for offline grid nesting in regional ocean models. Ocean Modell. 35, 1–15. http://dx.doi.org/10.1016/j.ocemod.2010.05.007.

Matsuyama, M., Iwata, S., Nagamatsu, H., 1997. Kyucho in Sagami Bay induced by Typhoon 8818. J. Oceanogr. 53, 199–205.

Marchesiello, P., McWilliams, J.C., Shchepetkin, A., 2003. Equilibrium structure and dynamics of the California current system. J. Phys. Oceanogr. 33, 753–783. http://dx.doi.org/10.1175/1520-0485(2003)33<753:ESADOT>2.0.CO;2.

Miyazawa, Y., Kagimoto, T., Guo, X., Sakuma, H., 2008. The Kuroshio large meander formation in 2004 analyzed by an eddy-resolving ocean forecast system. J. Geophys. Res. 113, C10015. http://dx.doi.org/10.1029/2007JC004226.

Miyazawa, Y., Zhang, R., Guo, X., Tamura, H., Ambe, D., Lee, J., Okuno, A., Yoshinari, H., Setou, T., Komatsu, K., 2009. Water mass variability in the Western North Pacific detected in 15-year eddy resolving ocean reanalysis. J. Oceanogr. 65, 737–756. http://dx.doi.org/10.1007/s10872-009-0063-3.

Mooney, P.A., Gill, D.O., Mulligan, F.J., Bruyère, C.L., 2016. Hurricane simulation using different representations of atmosphere–ocean interaction: the case of Irene (2011). Atmos. Sci. Let. 17, 415–421. http://dx.doi.org/10.1002/asl.673.

Morimoto, A., Kojima, S., Jan, S., Takahashi, D., 2009. Movement of the Kuroshio axis to the northeast shelf of Taiwan during typhoon events. Estuar. Coast. Shelf Sci. 82, 547–552. http://dx.doi.org/10.1016/j.ecss.2009.02.022.

Price, J.F., 1981. Upper ocean response to a hurricane. J. Phys. Oceanogr. 11, 153–175. http://dx.doi.org/10.1175/1520-0485(1981)011<0153:UORTAH>2.0.CO;2.

Pujol, I., Faugère, Y., Taburet, G., Dupuy, S., Pelloquin, C., Ablain, M., Picot, N., 2016. DUACS DT2014: the new multi-mission altimeter data set reprocessed over 20 years. Ocean Sci. 12, 1067–1090. http://dx.doi.org/10.5194/os-12-1067-2016.

Qiu, B., 2003. Kuroshio extension variability and forcing of the Pacific decadal oscillations: Responses and potential feedback. J. Phys. Oceanogr. 33, 2465–2482. http://dx.doi.org/10.1175/2459.1.

Qiu, B., Miao, W., 2000. Kuroshio path variations south of Japan: Bimodality as a self-sustained oscillation. J. Phys. Oceanogr. 30, 2124–2137. http://dx.doi.org/10.1175/1520-0485(2000)030<2124:KPVSOJ>2.0.CO;2.

Sakurai, T., Kurihara, Y., and Kuragano, T., 2005. Merged satellite and in-situ data global daily SST. in: Proceedings of the Int. Geoscience and Remote Sensing Symp., Seoul, South Korea, IEEE, pp. 2606–2608. doi: ⟨http://dx.doi.org/10.1109/IGARSS.2005.1525519⟩.

Schar, C., Smith, R.B., 1993. Shallow-water flow past isolated topography. Part II: Transition to vortex shedding. J. Atmos. Sci. 50, 1401–1412.

Shchepetkin, A.F., McWilliams, J.C., 2005. The regional ocean modeling system (ROMS): A split-explicit, free-surface, topography-following-coordinate oceanic model. Ocean Modell. 9, 347–404. http://dx.doi.org/10.1016/j.ocemod.2004.08.002.

Shchepetkin, A.F., McWilliams, J.C., 2008. Computational kernel algorithms for fine-scale, multiprocess, longtime oceanic simulations. In: Temam, R., Tribbia, J. (Eds.), Handbook of Numerical Analysis. Elsevier, Amsterdam, pp. 119–181. http://dx.doi.org/10.1016/S1570-8659(08)01202-0.

Sun, L., Yang, Y., Fu, Y., 2009. Impacts of typhoons on the Kuroshio large meander: Observation evidences. Atmos. Ocean. Sci. Lett. 2 (1), 45–50. http://dx.doi.org/10.1080/16742834.2009.11446772.

Sun, L., Yang, Y., Xian, T., Wang, Y., Fu, Y., 2012. Ocean responses to Typhoon Namtheun explored with Argo floats and multiplatform satellites. Atmos. Ocean. 50 (sup1), 15–26. http://dx.doi.org/10.1080/07055900.2012.742420.

Taguchi, B., Xie, S.P., Mitsudera, H., Kubokawa, A., 2005. Response of the Kuroshio extension to Rossby waves associated with the 1970s climate regime shift in a high-resolution ocean model. J. Clim. 18, 2979–2995. http://dx.doi.org/10.1175/JCLI3449.1.

Takeoka, H., Yoshimura, T., 1988. The kyucho in Uwajima Bay. J. Oceanogr. Soc. Jpn. 44, 6–16. http://dx.doi.org/10.1007/BF02303146.

Tanimoto, Y., Xie, S.P., Kai, K., Okajima, H., Tokinaga, H., Murayama, T., Nonaka, M., Nakamura, H., 2009. Observations of marine atmospheric boundary layer transitions across the summer Kuroshio Extension. J. Clim. 22, 1360–1374. http://dx.doi.org/10.1175/2008JCLI2420.1.

Tokinaga, H., Tanimoto, Y., Xie, S.P., Sampe, T., Tomita, H., Ichikawa, H., 2009. Ocean frontal effects on the vertical development of clouds over the western North Pacific: In situ and satellite observations. J. Clim. 22, 4241–4260. http://dx.doi.org/10.1175/2009JCLI2763.1.

Traon, P.Y.L., Nadal, F., Ducet, N., 1998. An improved mapping method of multisatellite altimeter data. J. Atmos. Ocean. Technol. 15, 522–534. http://dx.doi.org/10.1175/1520-0426(1998)015<0522:AIMMOM>2.0.CO;2.

Uchiyama, Y., Yoshiki, T., Tada, H., Baba, Y., Mizutani, H., Kubo, T., Mori, N., Saruwatari, A., Otsuka, J., Ninomiya, J., Watanabe, Y., Yamada, T., 2016. Upper-ocean dynamics and water-exchange at the entrance of a semi-enclosed bay under stratified and unstratified conditions. J. Jpn. Soc. Civil Eng. Ser. B2 (Coast. Eng.) 72 (2), 493–498 (in Japanese with English abstract).

Uchiyama, Y., Suzue, Y., Yamazaki, H., 2017a. Eddy-driven nutrient transport and associated upper-ocean primary production along the Kuroshio. J. Geophys. Res. Oceans 122. http://dx.doi.org/10.1002/2017JC012847.

Uchiyama, Y., Kanki, R., Takano, A., Yamazaki, H., Miyazawa, Y., 2017b. Mesoscale reproducibility in regional ocean modeling with a 3-D stratification estimate based on Aviso-Argo data. Atmosphere-Ocean 55, 1–18. http://dx.doi.org/10.1080/07055900.2017.1399858.

Rodriguez, E., Morris, C.S., Belz, J.E., Chapin, E.C., Martin, J.M., Daffer, W., Hensley, S., 2005. An Assessment of the SRTM Topographic Products. Jet Propulsion Laboratory, Pasadena, California, pp. 143.

Woodruff, S.D., Slutz, R.J., Jenne, R.L., Steurer, P.M., 1987. A comprehensive ocean-atmosphere data set. Bull. Am. Meteor. Soc. 68, 1239–1250. http://dx.doi.org/10.1175/1520-0477(1987)068<1239:ACOADS>2.0.CO;2.

Xue, Z., Zambon, J., Yao, Z., Liu, Y., He, R., 2015. An integrated ocean circulation, wave, atmosphere, and marine ecosystem prediction system for the South Atlantic Bight and Gulf of Mexico. J. Oper. Oceanogr. 8 (1), 80–91. http://dx.doi.org/10.1080/1755876X.2015.1014667.

Yang, B., Sheng, J., 2008. Process study of coastal circulation over the inner Scotian Shelf using a nested-grid ocean circulation model, with a special emphasis on the storm-induced circulation during tropical storm Alberto in 2006. Ocean Dyn. 58, 375–396. http://dx.doi.org/10.1007/s10236-008-0149-2.

Yang, Y., Sun, L., Liu, Q., Xian, T., Fu, Y., 2010. The biophysical responses of the upper ocean to the typhoons Namtheun and Malou in 2004. Int. J. Rem. Sen. 31 (17–18), 4559–4568. http://dx.doi.org/10.1080/01431161.2010.485140.